vehicles

MDPI

Article

Development and Verification of a FEM Model of Wheel–Rail Contact, Suitable for Large Parametric Analysis of Independent Guided Wheels

Manuel García-Troya *, Miguel Sánchez-Lozano and David Abellán-López

Department of Mechanical Engineering and Energy, Engineering Research Institute of Elche, Miguel Hernández University of Elche, Avda. de la Universidad, Edificio Innova, 03202 Elche, Spain; msanchez@umh.es (M.S.-L.); dabellan@umh.es (D.A.-L.)

* Correspondence: manuel.garciat@umh.es

Abstract

A quasi-static FEM framework for wheel–rail contact is presented, aimed at large parametric analyses including independently rotating wheel (IRW) configurations. Unlike half-space formulations such as CONTACT, the FEM approach resolves global deformations and strongly non-Hertzian geometries while remaining computationally tractable through three key features: (i) a tailored mesh transition around the contact patch, (ii) solver settings optimized for frictional contact convergence, and (iii) an integrated post-processing pipeline for creep forces, micro-slip, and wear. The model is verified against CONTACT, an established surface-discretization reference based on the Boundary Element Method (BEM), demonstrating close agreement in contact pressure, shear stress, and stick–slip patterns across the Manchester Contact Benchmark cases. Accuracy is quantified using error metrics (MAE, RMSE), with discrepancies analyzed in high-yaw, near-flange conditions. Compared with prior FEM-based contact models, the main contributions are: (i) a rigid–flexible domain partition, which reduces 3D computational cost without compromising local contact accuracy; (ii) a frictionless preconditioning step followed by friction restoration, eliminating artificial shear-induced deformation at first contact and accelerating convergence; (iii) an automated selection of the elastic slip tolerance (slto) based on frictional-energy consistency, ensuring numerical robustness; and (iv) an IRW-oriented parametrization of toe angle, camber, and wheel spacing. The proposed framework provides a robust basis for large-scale studies and can be extended to transient or elastoplastic analyses relevant to dynamic loading, curved tracks, and wheel defects.

Keywords: rolling contact; finite element method; wheel–rail contact; friction; wear optimization; independent guided wheels; independently rotating wheels

check for updates

Academic Editor: Jiliang Mo

Received: 24 July 2025
Revised: 11 September 2025
Accepted: 15 September 2025
Published: 19 September 2025

Citation: García-Troya, M.; Sánchez-Lozano, M.; Abellán-López, D. Development and Verification of a FEM Model of Wheel–Rail Contact, Suitable for Large Parametric Analysis of Independent Guided Wheels. *Vehicles* **2025**, *7*, 104. https://doi.org/10.3390/vehicles7030104

Copyright: © 2025 by the authors. Licensee MDPI, Basel, Switzerland. This article is an open access article distributed under the terms and conditions of the Creative Commons Attribution (CC BY) license (https://creativecommons.org/licenses/by/4.0/).

1. Introduction

The contact between the wheel and rail is a critical aspect in railway engineering, as it directly influences safety, comfort, energy efficiency, and the lifespan of train components. Accurate modeling of this contact is essential for predicting stresses, micro-slips, contact forces and wear.

Traditionally, Hertz's theory [1] has been the foundation for calculating contact stresses in elastic problems, based on the assumption that bodies are homogeneous and isotropic, with the contact patch having an elliptical shape. While this approach has proven effective in many applications, it has limitations when dealing with complex geometries, anisotropic

materials, or nonlinear loading conditions. To address these limitations, researchers like Hobbs [2] and Nayak et al. [3] expanded Hertz's theory, providing a deeper understanding of contact behavior under non-Hertzian conditions. Carter [4] introduced fundamental concepts about creep and friction forces in rolling contact. These contributions laid the foundation for the development of computational tools. Kalker [5] extended contact elasticity theory by incorporating more advanced models for nonlinear loads and tribological phenomena. His work has been implemented in software such as CONTACT [6], which has become a standard in wheel–rail contact analysis.

CONTACT implements Kalker's half-space theory through the Boundary Element Method (BEM). By discretizing only the contact surface instead of the full volume, it achieves high efficiency in solving elastic contact problems with friction and stick–slip. In addition to its static modules, CONTACT also provides quasi-dynamic and transient capabilities, with optimized formulations that make it particularly suitable for wheel–rail applications [6]. Nevertheless, the half-space formulation is inherently limited in its ability to capture global structural deformations, conformal contact near the flange, and material nonlinearities. In contrast, the Finite Element Method (FEM) discretizes the entire solid domain, providing a powerful, albeit computationally demanding, alternative to analytical and half-space-based approaches. Unlike the latter, FEM is not restricted by simplified geometries, linear elasticity, or limited material formulations [7–9]. It enables accurate prediction of stresses in regions where analytical models fail, such as the gauge corner or wheel flange [10]. Several studies have shown that the differences in predicted contact pressures between FEM and Hertzian-based methods can exceed the stresses in these critical areas [10,11]. Moreover, FEM models can incorporate complex contact conditions, elastoplastic material behavior, and velocity-dependent friction laws [12–14].

Despite these advances, many FEM models remain computationally expensive, particularly for large parametric studies or wear sensitivity analysis. In this work, a quasi-static FEM model with implicit time integration is proposed to evaluate pressures, shear stresses, and slip within the contact patch under loading conditions. The model is optimized to reduce computational cost while preserving accuracy in the predicted contact variables, as validated through comparison with the CONTACT software (version 23.2). Although dynamic and plasticity-enhanced FEM formulations exist, the objective here is to develop an efficient framework suitable for repeated simulations over a wide parameter space. This includes future work involving systematic variation in geometrical and loading parameters in independently rotating wheel (IRW) systems, for which this model will serve as a base.

IRW configurations present additional challenges due to the absence of torsional coupling between wheels and the potential for yaw instability [15,16]. The proposed FEM approach allows the parametric definition of geometric variables such as toe angle, camber angle, and internal wheel spacing. This is especially relevant for the rolling gear of independent guided wheels used in Talgo trainsets, where passive steering and radial guidance require specialized modeling strategies [17–19].

This work advances prior FEM-based wheel–rail contact models by combining: (i) a rigid–flexible domain partition, to cut 3D computational cost without sacrificing local contact accuracy; (ii) a frictionless preconditioning step followed by friction restoration to eliminate initial shear-induced deformation and accelerate convergence; (iii) an automated selection of the elastic slip tolerance (slto) based on quantitative frictional-energy consistency; and (iv) an extensible framework for analyzing the structural response of vehicle assemblies, in particular enabling the study of how contact forces are transmitted into suspension components and other substructures, thereby supporting integrated simulations of suspension systems under realistic operating conditions. The resulting quasi-static, implicit FEM achieves sub-percent errors in normal contact variables against CONTACT while

remaining suitable for large parametric sweeps. Moreover, the methodology establishes a platform that can be extended to transient analyses or explicitly integrated simulations in which dynamic effects and inertia become relevant—particularly in curved track scenarios or when simulating wheel defects—and to elasto-plastic formulations requiring full 3D fields (e.g., near flange/gauge corner, conformal contact, or material nonlinearity).

To contextualize the present FEM implementation, Table 1 contrasts it with representative 3D FE studies strictly aligned with our scope. Ref. [8] developed a 3D FE model in ANSYS (version 24.1) using measured profiles and highlighted the limitations of half-space assumptions at the gauge corner, reporting computation times of 48–60 h and large deviations with Hertz/CONTACT in conformal contact cases. Ref. [20] presented a static FE assessment focused on rail stress and safety under rolling, braking, and cornering loads, rather than on quasi-static rolling contact patch parametrics. More recent advances target complementary scopes: Ref. [21] validated a dynamic 3D FE model up to 10 kHz using the V-Track rig, while [22] experimentally validated a thermomechanical 3D FE model capturing flash temperatures at high slip ratios. In contrast, the present work focuses on a quasi-static rolling contact framework tailored for large parametric sweeps—rigid–flexible partition, frictionless preconditioning, and SLTO/FKT tuning—achieving an internal ~40% runtime reduction relative to our initial setup while preserving accuracy.

Table 1. Qualitative comparison of selected FEM studies on wheel–rail contact and the present work.

Study	Scope and Setup	Contact/Material Model	Rolling/Wear and Outputs	Computational Notes	Relevance vs. this Work
Telliskivi & Olofsson [8]	3D FEM in ANSYS with measured wheel–rail profiles; compared against Hertz and CONTACT; analyzed rail head and gauge corner	Elastic–plastic local response; highlighted half-space limitations in gauge corner	Contact patch and pressures; showed large deviations in gauge corner relative to Hertz/CONTACT	~40k nodes; ~2–3 days runtime; refined mesh in patch	Pioneering FEM with measured geometries; not designed for parametric sweeps; relevant to justify FEM in conformal contact
Zulkifli et al. [20]	Static 3D FEM rail–wheel model; stresses under rolling, braking, and cornering	Linear elastic; Coulomb $\mu = 0.3$	Rail stresses and safety factor; no parametric rolling contact	~200k nodes; loads up to 78 kN; wheel Ø965 mm	Focused on rail integrity, not on patch mechanics or stick–slip; complementary structural view
Zhang et al. [21]	Dynamic 3D FEM validated on V-Track up to 10 kHz	Elastic full-body model; validated with hammer tests and FRFs	High-frequency interaction, modal identification; not quasi-static	Extensive dynamic validation with experiments	Complements present model: strong dynamic validation vs. quasi-static parametric approach here
He et al. [22]	Thermo-mechanical 3D FEM; validated with infrared thermal imaging	Coupled thermo-mechanical; slip-dependent friction; T-dependent material	Flash temperatures (~360 °C) under high slip; <10% deviation vs. experiments	Implicit–explicit sequence; full-scale rig tests	Focus on thermal effects at high slip; different scope than current quasi-static wear-oriented FEM
Present work	Quasi-static 3D FEM in ANSYS; verified with Manchester Benchmark; parametric sweeps including IRWs	Augmented Lagrangian contact; rigid–flexible partition; frictionless preconditioning; automated slto tuning	Pressures, tractions, stick–slip, creep forces, wear (USFD); IRW parametrization	~40% faster than baseline FEM; 3 h/case on 20-core CPU; reproducibility via detailed settings	Provides a reproducible and efficient FEM workflow for large parametric studies, especially for IRWs

Notes: Computational times across studies are hardware- and setup-dependent and are not directly comparable; prior works rarely report standardized timings.

2. Materials and Methods

2.1. Modeling, Meshing and Boundary Conditions

ANSYS commercial software [23] is used to model the rolling contact between the wheel and rail.

To describe wheel modeling, a global coordinate system is adopted, as shown in Figure 1a:

X-axis is oriented in the longitudinal direction of vehicle advancement.
Y-axis is oriented in the lateral and rightward direction, perpendicular to the track.

Z-axis is established in the vertical and downward direction.

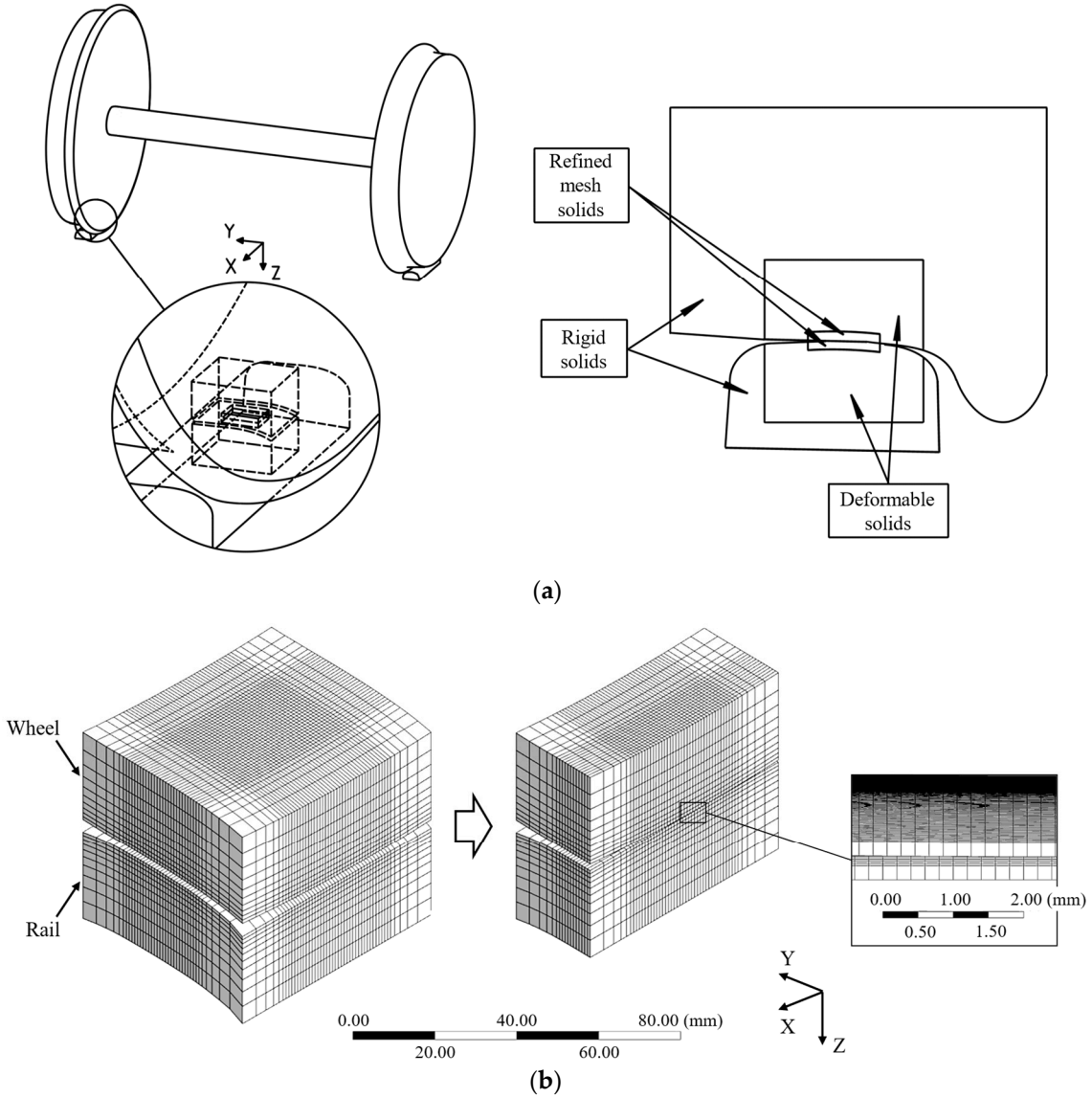


Figure 1. (**a**) Modeling of wheel–rail contact (S1002-UIC60); and (**b**) mesh detail and longitudinal sectional view of the solids at the right wheel–rail contact interface. Hexahedral elements with a size of 0.2 × 0.2 × 0.2 mm.

The origin of the global coordinate system is positioned on the track's symmetry plane, aligned with the highest points of the inclined rails. The contact modeling is illustrated for a rigid axle system using a S1002 wheel profile with taper 1/20 and a 60E2 rail profile inclined at 1/40.

To discretize both the wheel and rail, 8-node hexahedral elements are used. To achieve a balance between accuracy and computational cost, a non-uniform mesh is used, with finer elements at the contact zone.

The model consists of 11 solids: 3 rigid solids (excluded from the results) and 4 solids with a coarse mesh around the contact zones and refined where the contact patch is located, as seen in Figure 1b.

The geometrical discretization is performed with 0.2 mm elements where contacts occur. The result is approximately 500,000 nodes and 500,000 elements in each contact zone.

A slow mesh transition was applied between coarse and refined regions using local mesh controls and medium smoothing, to avoid abrupt size jumps and preserve

solution stability in the frictional contact. The contact patch and its vicinity were discretized hexahedrally.

Hexahedral 8-node linear elements with the Simplified Enhanced Strain (SES) formulation were used, which introduces internal modes to prevent shear locking without relying on reduced integration or hourglass control.

The approach focuses on studying phenomena near the contact area, simplifying the 3D model. The regions of the rail and wheels that are far from the contact area are modeled as rigid. As long as the elastic region is large enough to capture the non-negligible stress fields (typically extending beyond three times the contact patch dimensions), it is shown that the accuracy of the local contact stresses and strain energy distribution remains unaffected, as seen in Figure 2a.

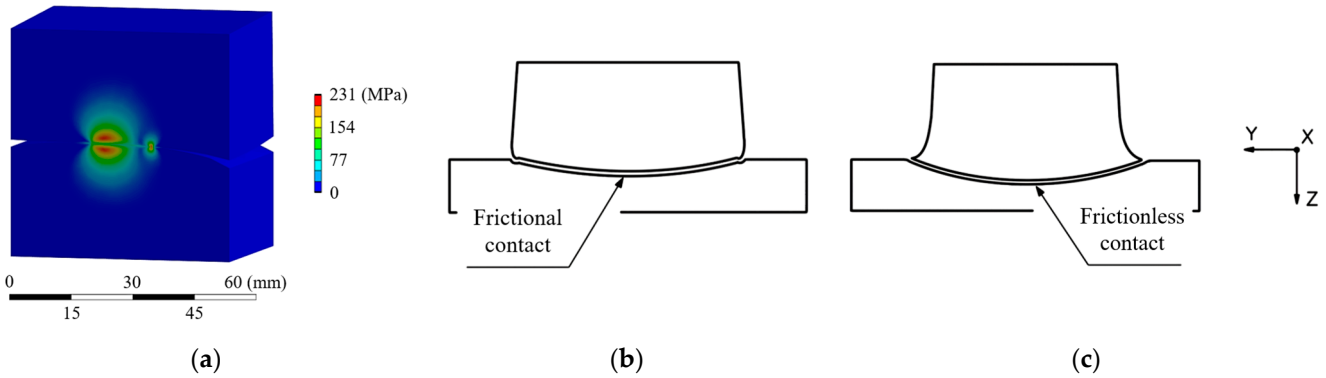


Figure 2. (**a**) Equivalent stress (Von Mises) in cross-sectional view; (**b**) comparison of deformation with friction; and (**c**) without friction at contact time (deformation factor $\times 2$).

This optimization strategy, combined with the selection of efficient numerical formulations, can reduce simulation time by up to 40%.

Regarding boundary conditions, the analysis is divided into five steps (Table 2):

(i) A vertical displacement is progressively applied to the axle to establish normal contact between wheel and rail. The vertical load is introduced gradually, with a non-zero friction coefficient.

(ii) Once contact is established, the vertical load is held constant while the friction coefficient is progressively reduced until it reaches zero.

(iii) The previously established conditions are maintained, ensuring that the contact patch readjusts to the frictionless contact state.

(iv) The contact friction coefficient is then set to its target (reference) value, with the contact patch already adapted to the rolling condition.

(v) Rolling motion is simulated by applying a constant longitudinal displacement to the wheel while allowing free rotation around the axle. The motion is constrained along the X-axis, and the vertical load is kept constant throughout the simulation.

Step (iii) addresses the deformations that arise when friction is present from the onset of contact, due to the accumulation of shear stresses (Figure 2b). Running this step without friction (Figure 2c) produces a deformation pattern governed solely by normal pressures, yielding a more representative initial state. Restoring the target friction coefficient in step (iv) then allows the rolling simulation (step v) to proceed under realistic conditions while reducing the additional distance otherwise required to reach convergence.

Table 2. Values of the boundary conditions and simulation time through the steps.

Step	Time (ms)	μ	FZ (kN)	Displacement (mm)	Spent Simulation Time (min)
1	0.15	0.3	0 to 20	0	8
2	0.3	0.3 to 0	20	0	6
3	0.45	0	20	0	5
4	0.6	0 to 0.3	20	0	5
5	10	0.3	20	0 to 18.8	158

When this strategy is not applied, the simulation requires a significantly longer rolling phase (step v) to reach convergence in the stress and deformation fields. Specifically, the rolling time increases by a factor of approximately two, as the contact patch needs to reconfigure itself progressively during rolling, starting from a deformed state induced by the initial frictional contact.

The values of the boundary conditions through the steps are shown in Table 2. In this configuration, the simulations achieve an average computation time of approximately 3 h per case, running on a 20-core CPU operating at 4.9 GHz. The average computation time per simulation step is approximately 8 min for the first step, 6 min for the second, 5 min for both the third and fourth steps, and 158 min for the final step, which involves the rolling analysis (Table 2).

The methodology presented would be applicable not only to rigid axle configurations but also to the rolling gear of independent guided wheels, allowing the analysis of the influence of variable geometric parameters such as toe angles (α), camber angles (β), wheel spacing, and other geometry configurations (Figure 3).

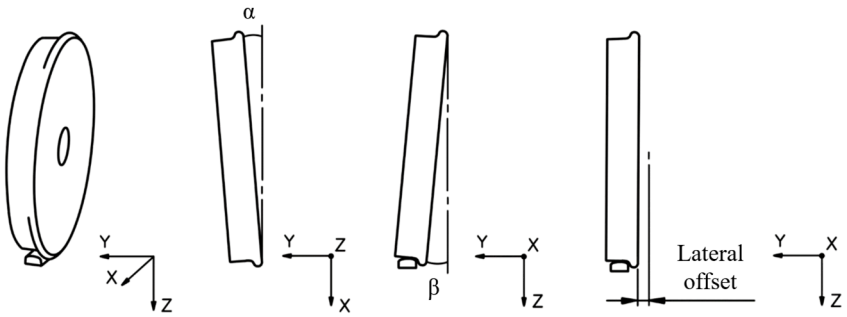


Figure 3. Parameterizable configurations of future models.

2.2. Mesh Sensitivity

To evaluate the influence of mesh resolution on the numerical results, a mesh sensitivity analysis was performed by comparing three different element sizes in the contact region: 0.8 mm, 0.4 mm, and 0.2 mm. Table 3 summarizes the main output variables of interest: maximum contact pressure, maximum contact shear stress, contact area, and sliding indication.

The results show a negligible variation in contact pressure across mesh sizes, with a maximum deviation of only 1.1% between the coarsest (0.8 mm) and the finest mesh (0.2 mm). Contact shear stress is more sensitive to mesh refinement, exhibiting an increase of 8.5% from 0.8 mm to 0.4 mm and 2.9% from 0.4 mm to 0.2 mm. This suggests that the shear stress field benefits more from local refinement near the contact surface.

The contact area remains practically unaffected by mesh size, with differences below 0.4%. Similarly, the sliding indication is fully stable across all mesh configurations, indicating that the tangential kinematics are well captured even with coarser meshes.

Table 3. Influence of mesh size on contact parameters in the wheel–rail model (Case 1).

Mesh Size (mm)	**0.8**	**0.4**	**0.2**
Contact pressure (MPa)	333.8	335.0	338.7
Percentage difference (%)	-	0.4	1.1
Contact shear stress (MPa)	86.8	94.9	97.7
Percentage difference (%)	-	8.5	2.9
Contact area (mm^2)	50.6	50.7	50.9
Percentage difference (%)	-	0.2	0.4
Sliding indication (-)	0.081	0.081	0.081
Percentage difference (%)	-	0.0	0.0

Based on these results, the mesh with an element size of 0.2 mm was selected for the final simulations, as it provides the highest level of accuracy while maintaining numerical stability in all contact variables.

2.3. Model Formulation and Control

2.3.1. Contact Model

The normal contact problem in the wheel–rail interaction is solved using the Augmented Lagrangian Method [24].

The frictional state of each node follows Coulomb's law: adhesion holds when $\|\tau\| \leq \mu\, p_n$, while sliding occurs if $\|\tau\| > \mu\, p_n$, where τ is the contact shear stress vector and p_n is the local contact pressure.

The CONTA174 element is used to model contact between surfaces [25]. The contact is asymmetrical to reduce the computational cost, defining the wheel as master and the rail as slave.

The tangential contact stiffness is modeled as follows:

$$K_t = F_{K_t} \cdot \mu \cdot \frac{p_n}{slto} \quad (1)$$

where

K_t is the tangential stiffness;
F_{K_t} is the tangential stiffness factor;
μ is the friction coefficient;
p_n is the contact pressure;
slto is the elastic slip tolerance.

In this work the results are compared with previous reference cases of the rigid axle [26,27]. The objective is to reproduce the stick and slip zones, which is achieved by balancing an increase in tangential contact stiffness and the prevention of chattering.

To obtain accurate results in both the adhesion and slip regions, as well as in the evaluation of tangential contact stress, the elastic slip tolerance parameter is adjusted according to the following expression:

$$slto = S_{tol} \cdot l_i \quad (2)$$

where S_{tol} is the dimensionless slip tolerance factor, and l_i is the characteristic contact length associated with the size of the finite element.

Typical values of S_{tol} range from 0.005 to 0.0002, depending on the sensitivity of the model. A value that is too high may lead to significant inaccuracies in the estimation of

frictional dissipation, while a value that is too low may negatively impact the convergence behavior of the solver [28].

Therefore, S_{tol} is treated as a tuning parameter and should be adjusted through parametric analysis, seeking a balance between numerical convergence and the accuracy of energy dissipation estimation in the contact interface. Based on this trade-off and the required level of accuracy, a value of 0.00025 was selected. This choice is supported by the results obtained for dissipated energy in the contact region (Figure 4), showing an error of approximately 2% with respect to the accumulated frictional dissipated energy compared to the next configuration. This approach provides a practical way to automate the selection of the elastic slip tolerance (slto) parameter based on quantitative energy dissipation criteria.

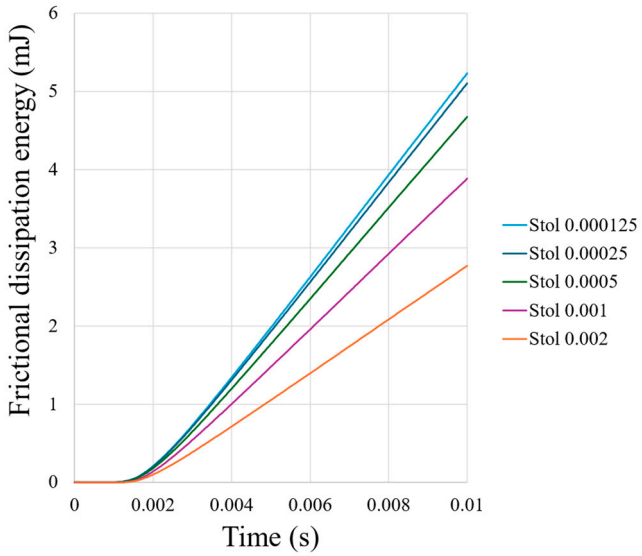


Figure 4. Influence of elastic slip tolerance on frictional dissipation energy.

2.3.2. Integration Model and Instability Control

The integration scheme is implicit and follows a quasi-static approach in ANSYS Static Structural. A nonlinear iterative solution method is used, specifically the Newton-Raphson algorithm [29,30]. Improper discretization can lead to numerical errors, affecting the normal and tangential contact solution.

A common issue in rolling contact simulations is numerical instability, manifesting as spurious oscillations in the contact shear stress profile. To control this, Equation (3) is used:

$$c = \frac{\delta q}{\delta x} \tag{3}$$

where c represents the ratio of rolling displacement per time increment (δq) to mesh size (δx) [6]. An inappropriate c can lead to unstable tangential force calculations.

In half-space theory models, spatial and temporal discretization requires $c \geq 1$ to maintain numerical stability [7,31]. However, in FEM models, selecting $c \leq 1$ provides a balance between accuracy and efficiency.

Thus, the time increment for each integration substep is calculated as follows:

$$\delta t = \frac{1}{V} \cdot \delta q \tag{4}$$

where V is the rolling velocity. In this study, with a mesh size of 0.2 mm and a rolling velocity of 2 m/s, the time increment must be less than 0.1 ms.

Full solver settings, including the exact time stepping values, contact formulation options, and numerical controls employed in ANSYS, are compiled in Supplementary Table S1 for reproducibility.

A flowchart of the modeling methodology is provided in Figure 5, summarizing the main steps from geometry definition to verification. The figure details all substeps of the workflow, including meshing strategy, material properties, five-step loading sequence, contact formulation, solver settings, post-processing routines, and wear calculation.

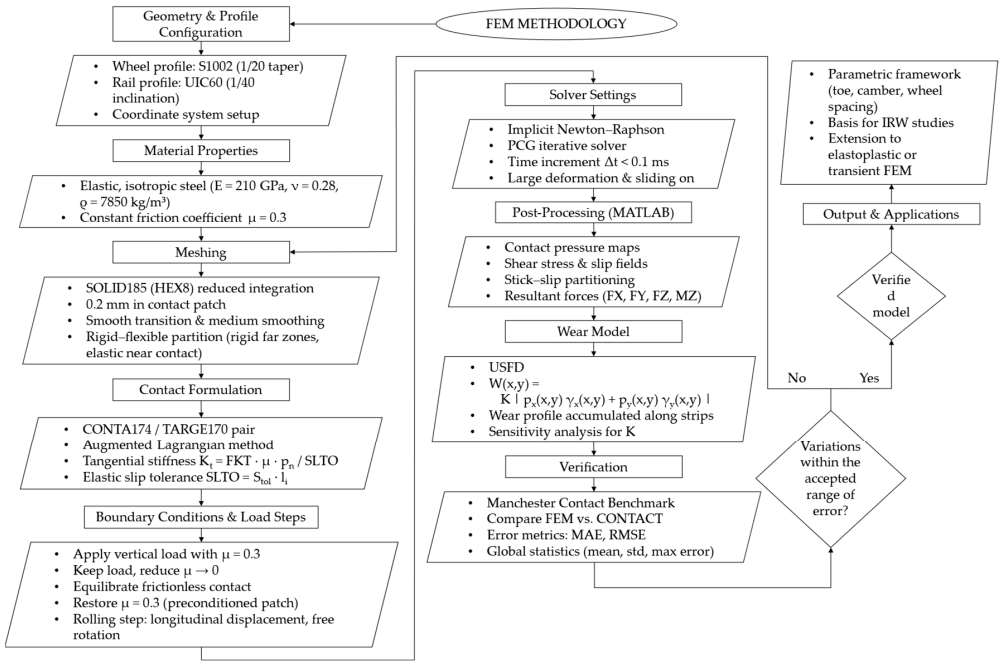


Figure 5. Flowchart of the proposed FEM for wheel–rail contact simulations.

2.4. Results Generation and Post-Processing

The developed model provides substantial flexibility for wheel–rail contact analysis, enabling: (i) modification of geometric, meshing, and numerical parameters to adapt to diverse study conditions; (ii) detailed evaluation of contact pressure, shear stress, and slip distributions within the patch; (iii) post-processing to derive secondary quantities—such as wear—for design optimization and parametric comparison; and (iv) construction of simulation matrices (design of experiments) by systematically varying geometric and control parameters to conduct sensitivity studies.

2.4.1. Normal Problem

The distributions of contact pressures under the applied loading conditions are obtained and post-processed in MATLAB R2023a. Figure 6 shows examples of the results for different cases, illustrating the pressure magnitudes and patch dimensions.

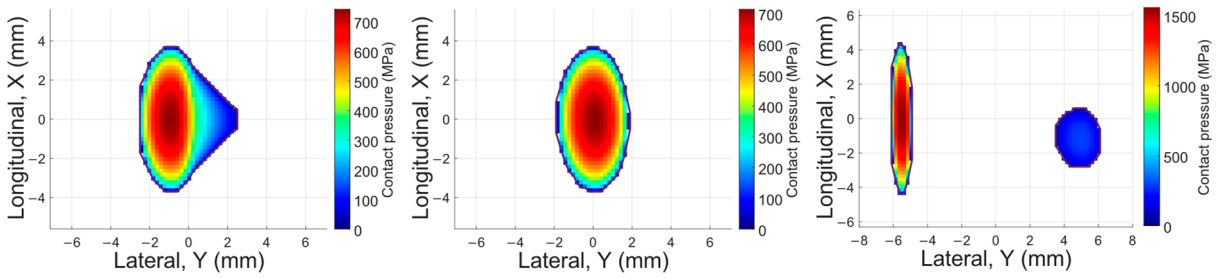


Figure 6. Contact pressure results obtained for different case studies.

2.4.2. Tangential Problem

Tangential results—namely shear stress distribution, slip, and stick–slip partitioning—are directly obtained from the contact formulation of Section 2.3.1 and subsequently post-processed in MATLAB R2023a. Figure 7 illustrates representative outputs of these quantities.

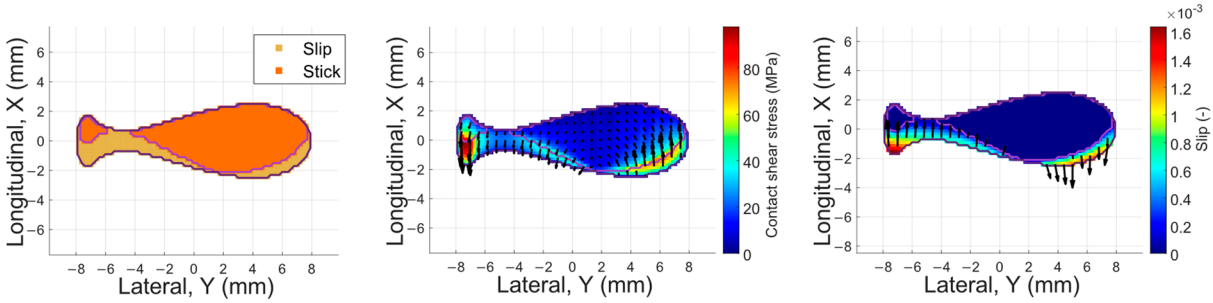


Figure 7. Tangential problem results. Stick-slip zones, contact shear stress distribution, and slips.

2.4.3. Force Calculation

The integration of contact pressure and shear stress distributions allows the calculation of the resultant forces in the normal and tangential directions, which are computed using the following equations:

$$F_X = \sum_I \left(p_I^X \delta_X \delta_Y \right) \tag{5}$$

$$F_Y = \sum_I \left(p_I^Y \delta_X \delta_Y \right) \tag{6}$$

$$F_Z = \sum_I \left(p_I^Z \delta_X \delta_Y \right) \tag{7}$$

$$M_Z = \delta_X \delta_Y \sum_I \left(p_I^Y X_I - p_I^X Y_I \right) \tag{8}$$

where

F_X, F_Y, F_Z are the forces in the longitudinal, lateral, and normal directions within the contact patch;
M_Z is the spin moment within the contact patch;
p_I^X, p_I^Y, p_I^Z are the contact shear stresses at node I in the X, Y, and Z components;
$\delta_X \cdot \delta_Y$ is the element area, the product of its dimensions in the X and Y directions;
X_I, Y_I are the distances to the moment application point for node I in the X and Y components.

These magnitudes provide a global measure of contact behavior and are critical for verifying the model.

2.4.4. Wear Calculation

Among the most used wear models are: USFD, KTH, and BRR. The USFD model is accurate for specific materials and mixed contact (stick-slip) scenarios [32,33].

This model is an empirical approach that correlates the dissipated energy at the wheel–rail interface with the mass wear rate. It classifies wear into three regimes (mild, severe, and catastrophic) allowing for an evaluation of wear distribution and friction effects. It computes wear based on local tangential force and slips within the contact patch, using an experimentally determined wear coefficient K specific to the material. The wear rate is defined as shown in the following equation:

$$W(x,y) = K \frac{T\gamma}{A}(x,y) = K \left| p_x(x,y)\gamma_x(x,y) + p_y(x,y)\gamma_y(x,y) \right| \tag{9}$$

where

W is the local mass wear rate ($\mu g/m_{rolled}/mm^2$);
K is the empirical wear coefficient specific to the material [32];
T is the local tangential force (N);
γ_x, γ_y are the local slip values (dimensionless) in the X and Y directions;
A is the local contact area (mm^2);
p_x, p_y are the contact shear stresses in the X and Y directions.

The wear coefficient (K), depending on the wear regime, takes specific values obtained experimentally from twin-disc tests using R8T steel for the wheel and UIC60 900A steel for the rail, as described in [32,33].

The mass wear rate is calculated, for each element of the contact patch, using the results of contact shear stress distribution and slips of Section 2.4.2. Subsequently, elemental contributions are summed for each strip across the entire contact patch, resulting in a cumulative wear profile, as given in Equation (10). This method is shown schematically in Figure 8.

$$D_j = \frac{1}{\rho}(V\Delta t)\frac{\Delta x_j}{2\pi R_j}\sum_{i=1}^{N} W_{i,j} \quad (10)$$

where

i is the position of the element in the strip;
j is the longitudinal strip;
ρ is the material density;
VΔt is the distance travelled (rolling);
Δx_j is the dimension of the element in the longitudinal and lateral directions;
R_j is the rolling radius;
D_j is the wear depth in strip j per rolling distance.

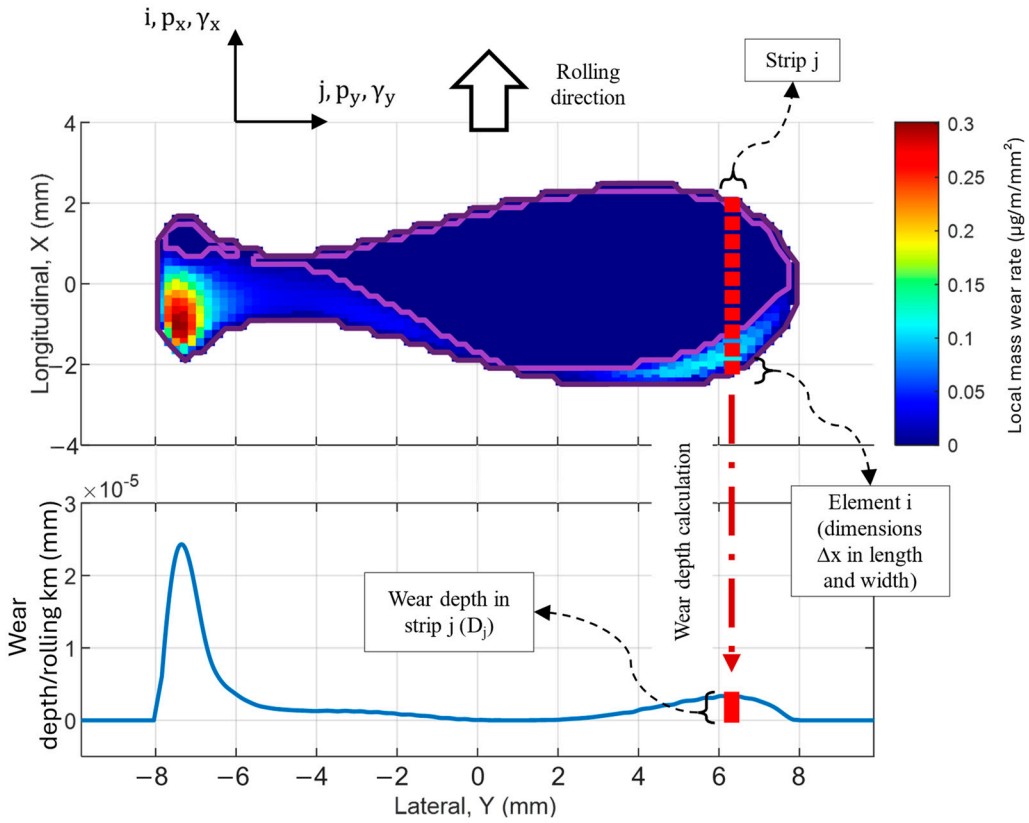


Figure 8. Schematic representation of the method for obtaining wear depth using USFD model.

Sensitivity to the USFD coefficient K was assessed by scaling K by factors {0.5, 1.0, 2.0}. While absolute wear magnitudes scaled linearly, the spatial distribution, peak locations, and relative rankings across cases remained invariant. Consequently, K is kept constant here and wear is interpreted comparatively; material-specific calibration is planned in future work.

2.4.5. Mesh and Profile Update Strategy

In this study, the mesh and wheel profile are not updated during simulation because the wear predicted per run is an order of magnitude smaller than the characteristic mesh size of the contact region and therefore insufficient to distort the geometry or compromise stress and slip accuracy. This is consistent with literature recommendations: [34] suggests updating profiles only when wear exceeds 0.1 mm in depth, while [35] advises a minimum of 50 km of rolling before re-evaluating the geometry. Since the present simulations cover only a few wheel rotations, the accumulated wear remains well below these thresholds, and neglecting profile or mesh updates avoids unnecessary remeshing and computational overhead without improving accuracy.

For completeness, Supplementary Table S1 compiles geometry, materials, mesh design (including transition/smoothing), contact settings, and solver controls, enabling full reproducibility.

3. Verification of the Modeling Methodology

The Manchester Contact Benchmark [26] is employed to verify the results of the FEM model for normal and tangential contact. This benchmark consists of a set of test cases designed to evaluate and compare simulation models for wheel–rail contact. Case A is used, which considers a single wheelset with specific loading and geometric conditions, enabling a direct comparison of the FEM model with results obtained using various reference software tools [27].

The wheelset model is illustrated in Figure 9 (left), along with its nominal radius. The simulations use actual wheel profiles (S1002) and rail profiles (UIC60) with a 1:40 inclination. A friction coefficient of $\mu = 0.3$, a vertical load of 20 kN, and a forward velocity of 2 m/s are considered.

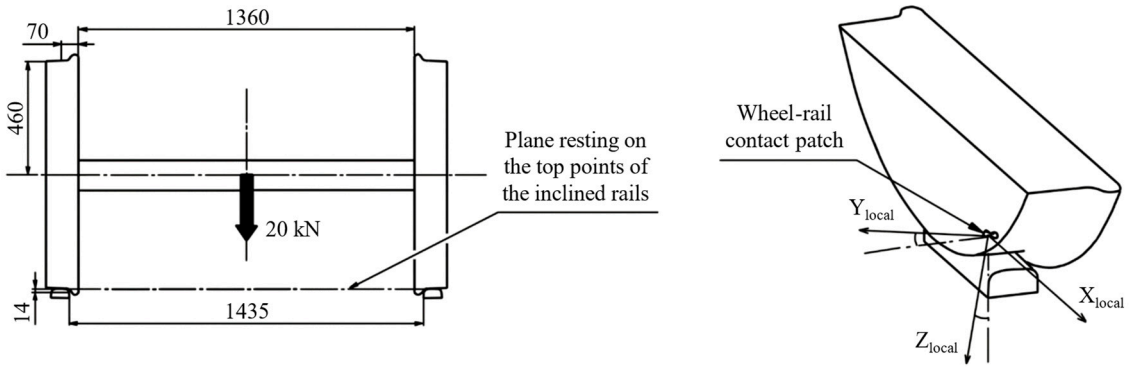


Figure 9. Illustration of the single wheelset model used in the Manchester Contact Benchmark simulation, Case A [26] (**left**). Representation of the local coordinate system (**right**).

The results are presented using a local coordinate system (Figure 9, right), whose origin is located at the center of the wheel–rail contact patch and is tangent to the surfaces at that point.

The lateral displacement varies from 0 to 10 mm (Figure 10) in increments of 0.5 mm, while the yaw angle increases from 0 to 24 mrad in steps of 1.2 mrad (21 cases). In this study, only odd cases are analyzed (Table 4).

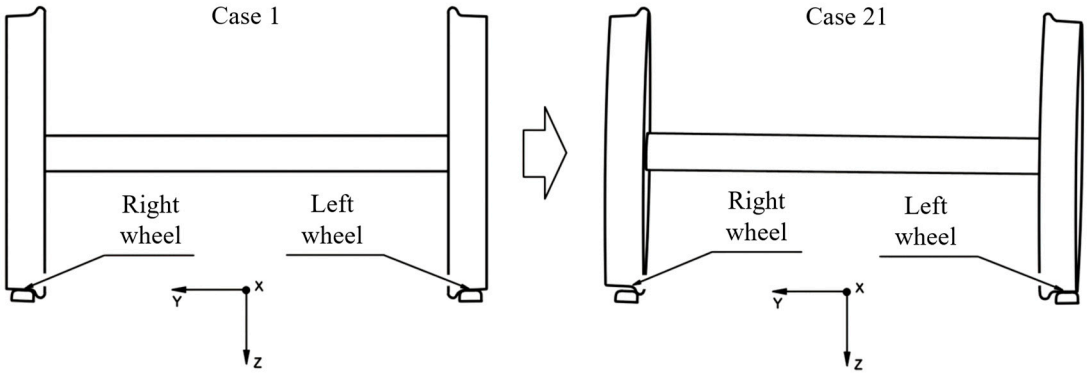


Figure 10. Representation of the rigid axle configuration (lateral displacement and yaw angle). From Case 1 (initial) to Case 21 (final).

Table 4. Lateral displacements and yaw angles of each case number of Manchester Contact Benchmark [26].

Lateral Displacement of the Wheelset CoG (mm)	**0**	**1**	**2**	**3**	**4**	**5**	**6**	**7**	**8**	**9**	**10**
Yaw angle (mrad)	0	2.4	4.8	7.2	9.6	12	14.4	16.8	19.2	21.6	24
Case number	1	3	5	7	9	11	13	15	17	19	21

The geometric and mechanical properties of the model are summarized in Table 5.

Table 5. Values of the test model parameters.

Parameter	**Value**
Vertical load per wheel	10 kN
Linear velocity	2 m/s (7.2 km/h)
Young's modulus	210 GPa
Poisson's ratio	0.28
Density	7850 kg/m^3
Friction coefficient	0.3
Wheel diameter	920 mm
Rail head radius	300 mm
Wheel conicity	1/20
Rail inclination	1/40

The material law used was linear elastic, isotropic, and temperature-independent, excluding plasticity, damping, and thermal dependencies. This is consistent with the scope of elastic contact validation against CONTACT.

3.1. Solution of the Normal Contact Problem

This section presents the distribution of contact pressures and compares the results obtained using CONTACT and FEM, analyzing the differences between both methods and their impact on the accuracy of the simulation. All results presented in this section correspond to the last substep of the simulation, when the system has reached a stable state.

Table 6 provides a comparison between CONTACT and FEM in terms of contact patch dimensions and maximum contact pressure values.

Table 6. Comparison between methods (CONTACT-FEM)—Case 1, right wheel.

Solution	Semi-Axis a (mm)	Semi-Axis b (mm)	Area (mm^2)	Maximum Contact Pressure (MPa)
FEM	2.39	7.85	52.83	338.7
CONTACT	2.40	7.80	51.64	338.3
% Difference vs. CONTACT	0.5%	0.6%	2.3%	0.1%

The results show that both methods provide comparable values, with differences in the contact area below 2.3% and a variation in the maximum contact pressure of 0.1%. These discrepancies fall within the expected margins for nonlinear contact simulations and are consistent with the typical numerical approximations present in FEM and analytical contact models. The same trend is observed in tangential contact results, where slight variations in stick-slip zones, contact shear stresses, and slip distributions are expected due to methodological differences between FEM and CONTACT.

Figure 11 illustrates the distribution of contact pressure in the contact patch obtained with both models. Figure 12 presents this distribution for the longitudinal section of the contact patch where the maximum contact pressure is located.

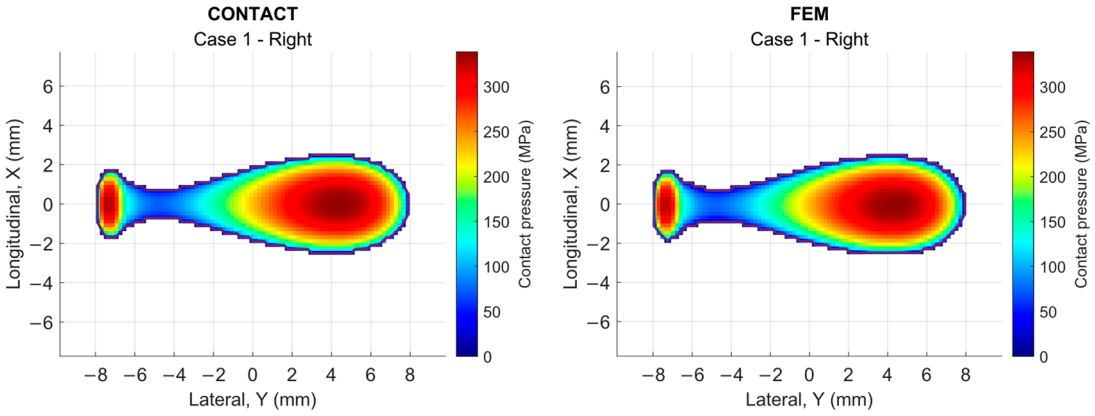


Figure 11. Contact pressure distribution in the contact patch. CONTACT-FEM comparison.

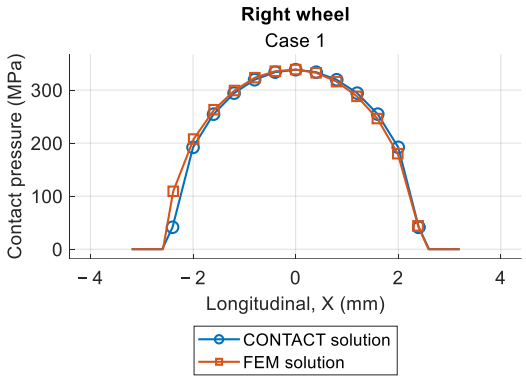


Figure 12. Longitudinal section view of the contact pressure distribution. CONTACT-FEM comparison.

One of the most relevant aspects of this case study is the presence of two local maxima in the contact patch, a characteristic that does not occur in all configurations. In the area closest to the wheel flange (corresponding to negative values on the Y-axis), the values obtained with FEM tend to be slightly lower than those calculated with CONTACT, with 324.9 MPa in the first case and 328.2 MPa in the second, representing a variation of −1%.

In the region further from the flange (corresponding to positive Y-axis values), higher pressure values are observed in both models due to an increase in interface penetration. However, the maximum contact pressure values are nearly identical, with 338.7 MPa in the FEM model and 338.3 MPa in CONTACT, corresponding to a difference of 0.1%, as shown in Table 6.

This analysis is based on Case 1 (right wheel). Detailed per-case errors for contact patch dimensions and pressures are reported in Supplementary Tables S2 and S3, while global statistics (mean, standard deviation, maximum error) are summarized in Supplementary Tables S4 and S5.

Additional cases and their corresponding results are provided in Supplementary Sections S5 and S6.

3.2. Solution of the Tangential Contact Problem

The tangential problem in wheel–rail contact is directly related to the transfer of forces, as well as the mechanisms of wear at the interface. In particular, the tangential interaction determines the stress distribution, the differentiated stick and slip zones, and the relative displacements between the contacting surfaces.

This section presents the results obtained for stick and slip zones, the distribution of contact shear stresses, and slips, comparing the FEM and CONTACT solutions.

3.2.1. Stick/Slip Zones

The FEM model predicts an adhesion area of 37.0 mm^2 compared with 37.7 mm^2 in CONTACT, corresponding to 1.9% relative error. Adhesion is concentrated at the front of the contact patch, while slip occurs toward the rear, in agreement with the expected rolling-contact behavior. Figure 13 compares the FEM and CONTACT predictions, showing consistent partitioning of stick and slip zones across the patch.

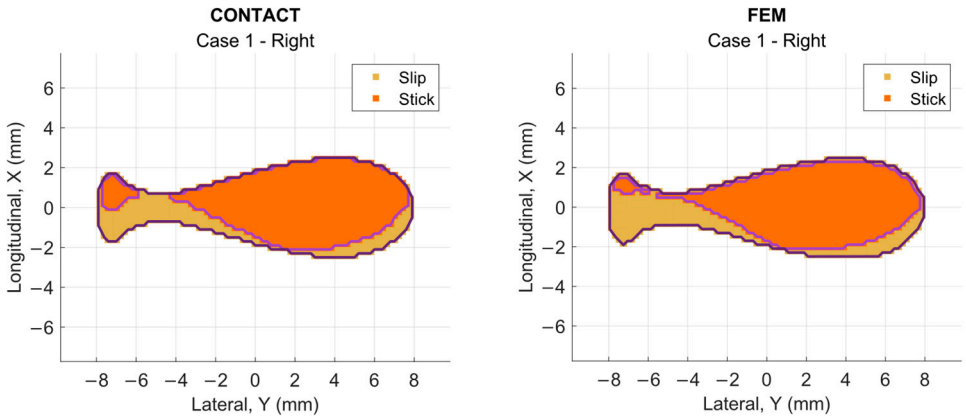


Figure 13. Stick-slip area distribution in the contact patch. CONTACT-FEM comparison.

One of the most critical factors contributing to the differences between FEM and CONTACT is that, in the FEM model, the solids elastically deform under the contact forces globally. This means that the contact shear stresses and pressures are distributed differently along the contact patch due to elastic deformation of the material. In CONTACT, solids are treated as rigid bodies (with a simplified local elasticity), which reduces the complexity of the contact problem. However, in FEM, the elastic deformation of the bodies results in a redistribution of forces as the geometries of the contacting surfaces adjust (Section 2.1).

The observed differences in stick-slip zones follow the same pattern as those discussed in Section 3.1, with deviations within the expected range for nonlinear contact models.

These results correspond to Case 1, right wheel. For other cases, the results are provided in Supplementary Section S7.

3.2.2. Contact Shear Stresses

Figure 14 presents the CONTACT-FEM comparison of the contact shear stress distribution within the contact patch. It is observed that stress concentration tends to shift towards the rear section of the contact patch under rolling conditions.

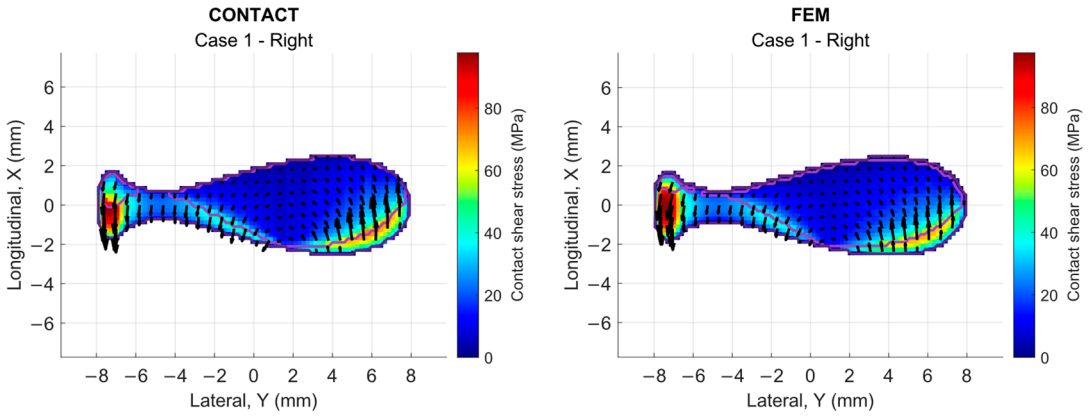


Figure 14. Contact shear stress distribution in the contact patch. CONTACT-FEM comparison.

The effect of spin is significant in the orientation of contact shear stress vectors, generating an asymmetric arrangement due to the wheel conicity. This asymmetry in the contact patch is reflected in the stress distribution, which exhibits different behaviors on the right and left sides of the contact patch with respect to the X-Z plane. This pattern is consistent with previous rolling contact studies, where spin plays a crucial role in stress distribution.

The vectors are arranged in a counterclockwise direction (for the case of right wheel contact), and their magnitude depends on the loading conditions and contact geometry, which aligns with the expected behavior in wheel–rail contact analysis. The comparison demonstrates a strong correlation in stress values between both methods, with a difference of less than -0.2% in maximum values (97.5 MPa in FEM vs. 97.7 MPa in CONTACT).

Figure 15 shows the comparison of contact shear stress values corresponding to the longitudinal section of the contact patch where the maximum contact pressure is located. The maximum possible value, corresponding to full slip conditions, is found at $X < -2$. A good correlation is observed between CONTACT and FEM results.

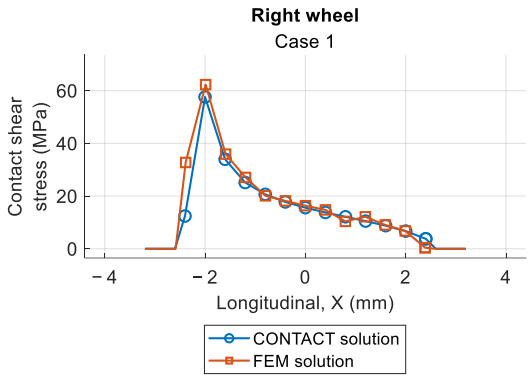


Figure 15. Longitudinal section view of the contact shear stress distribution. CONTACT-FEM comparison.

The results interpretation is based on Case 1, right wheel. The results for the other cases are provided in Supplementary Sections S8 and S9.

3.2.3. Slip Distributions

Figure 16 presents the slip distribution obtained using FEM and its comparison with the results generated by CONTACT. The slip values can be cross-referenced with the graphs in the previous sections, where the stick-slip zones (Figure 13, Section 3.2.1) and contact shear stresses analyzed. As expected, zero slip values are observed in the stick region, while in areas where contact shear stresses are higher (Figure 14, Section 3.2.2), slip increases.

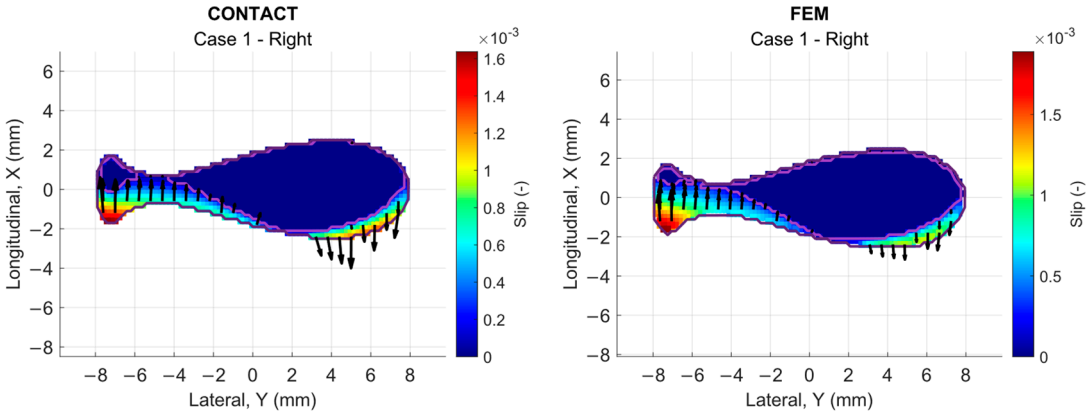


Figure 16. Slip distribution in the contact patch. CONTACT-FEM comparison.

The comparison between FEM and CONTACT results reveals a significant correlation in both the magnitude and direction of slip vectors. This suggests that the FEM model provides consistent results in terms of spatial distribution and intensity of the slip phenomenon, with a maximum slip value of 0.18% for FEM and 0.16% for CONTACT.

Figure 17 shows the slip distribution along the longitudinal axis (X-axis) for the contact patch strip where the maximum contact pressure occurs, comparing both methods.

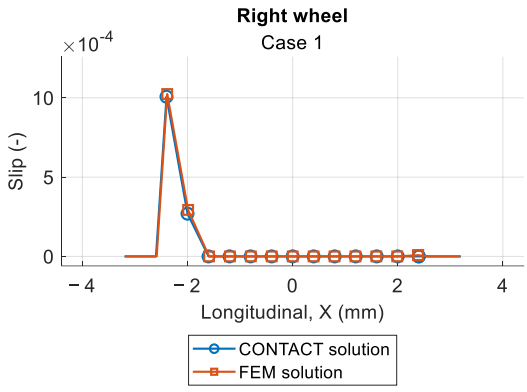


Figure 17. Longitudinal section view of the slip distribution. CONTACT-FEM comparison.

The results presented correspond to Case 1, right wheel. Stick–slip partitioning and shear stress errors are provided in Supplementary Tables S2 and S3, with statistical summaries in Supplementary Tables S4 and S5.

The results for the other cases are provided in Supplementary Sections S10 and S11.

3.3. Resultant Forces

As discussed in Section 3, the lateral displacements are adjusted in increments of 1 mm, while the yaw angles are modified in increments of 2.4 mrad [26,27]. The forces and

moments obtained using the FEM model are compared with those from CONTACT, with all values referenced to the local coordinate system of the contact patch (Figure 9, right).

Figure 18 presents the longitudinal force values, obtained using Equation (5). The results show differences of less than 5.1% for contact in both wheels, with maximum differences occurring in Cases 3 and 11 (left and right wheels, respectively).

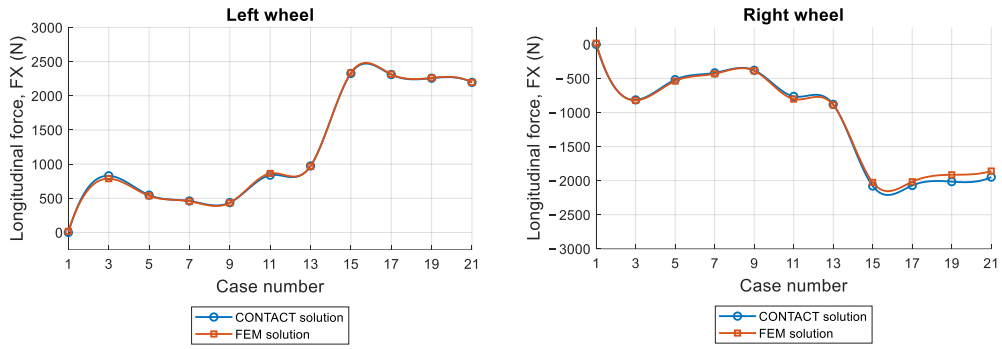


Figure 18. Comparison of CONTACT-FEM longitudinal force results for each test case. Left wheel (**left**) and right wheel (**right**).

For lateral forces, obtained using Equation (6), the highest percentage variations occur in Cases 15 (left wheel) and 19 (right wheel), as shown in Figure 19. These deviations occur primarily because the contact patch in these cases is positioned near the flange (right wheel). However, even in these conditions, for the left wheel, the error does not exceed 1.7%, while for the right wheel, the error remains below 4.3% in all cases.

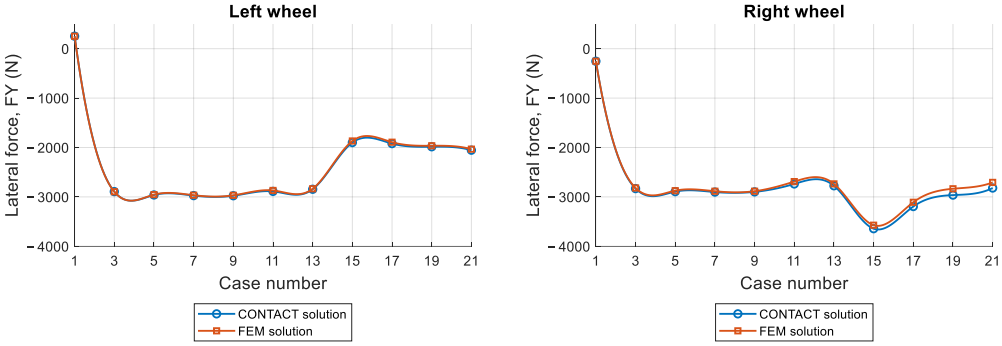


Figure 19. Comparison of CONTACT-FEM lateral force results for each test case. Left wheel (**left**) and right wheel (**right**).

The longitudinal and lateral (tangential) forces present the greatest level of complexity in terms of accuracy, which is associated with the formulation and mechanics of the tangential problem in this type of contact analysis (as mentioned in previous sections).

For the normal solution, obtained using Equation (7), all results exhibit a percentage error below 0.5% for the left wheel (Figure 20). For the right wheel, errors remain below 3%, except in Cases 19 and 21, where the deviations are below 4.3%.

Figure 21 presents the comparison of spin moment results in the contact patch, obtained using Equation (8).

The analysis of all cases revealed a pattern: percentage errors tend to increase in later cases, especially in the right wheel contact. The differences between the FEM and CONTACT results in cases where contact is located on the wheel flange can be explained by differences in the assumptions and capabilities of both approaches.

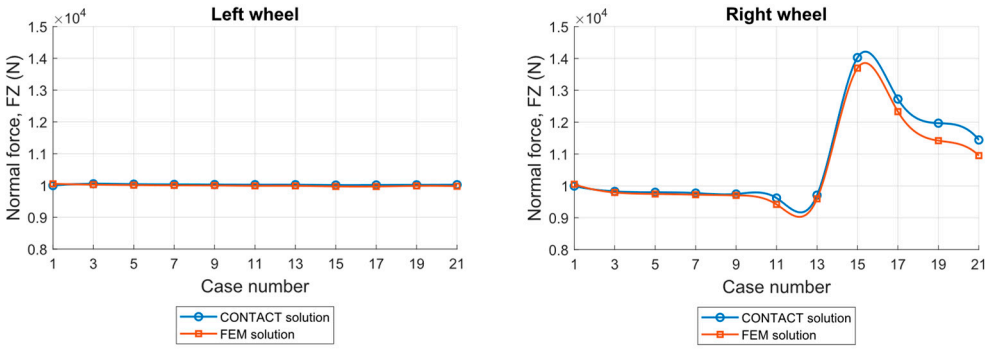


Figure 20. Comparison of CONTACT-FEM normal force results for each test case. Left wheel (**left**) and right wheel (**right**).

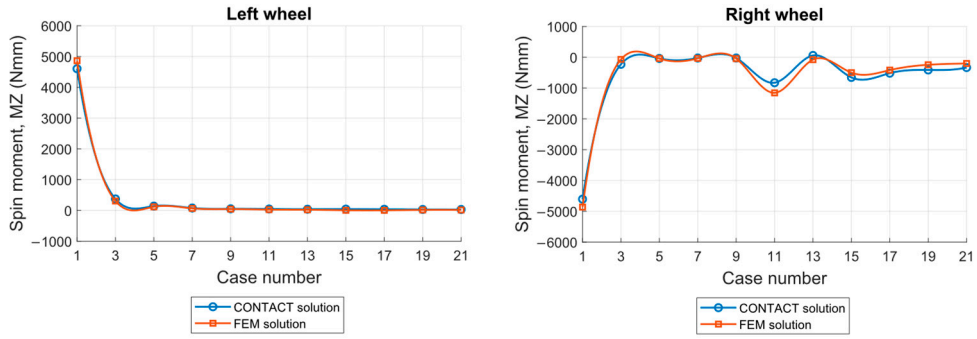


Figure 21. Comparison of CONTACT-FEM spin moment results for each test case. Left wheel (**left**) and right wheel (**right**).

Analytical models based on the elastic half-space theory rely on strict assumptions—such as homogeneity, isotropy, and a contact patch significantly smaller than the local radii of curvature—which are not valid in certain regions, especially near the wheel flange or gauge corner. In these areas, the curvature radii can be small, making the half-space assumption questionable [10].

Comparative studies have shown that while half-space-based methods provide acceptable results under standard head contact conditions, they can lead to significant errors near the flange. In some cases, the estimated contact pressure may exceed expected values compared to FEM simulations [8,10]. FEM is not constrained by this assumption, allowing it to capture local contact characteristics more accurately, though at a higher computational cost and with potential numerical sensitivities.

Furthermore, FEM allows for the modeling of complex contact conditions, including phenomena beyond the reach of simplified analytical models [36]. These capabilities are particularly relevant when analyzing stress distributions, adhesion–slip transitions, and energy dissipation near the flange area under lateral loading.

The full set of force and moment errors across all cases is reported in Supplementary Tables S2 and S3, confirming stable agreement with CONTACT except in high-yaw, near-flange cases.

3.4. Wear Analysis

3.4.1. Qualitative Analysis

The distribution of contact shear stresses and slip zones enables the identification of critical wear areas in the wheel–rail interface. The highest stresses and slips are concentrated in the rear section of the contact patch, where dominant slip occurs, leading to greater energy dissipation and increased wear rates. Additionally, when the contact patch shifts

toward the wheel flange, the local stress concentration rises due to the higher geometric curvature, further increasing wear in these regions.

3.4.2. Quantitative Analysis

The local implementation of the USFD model is performed by discretizing the contact patch into elements and computing the dissipated energy in each one based on the local contact shear stresses and relative slip obtained from the FEM model (Figure 8), as explained in Section 2.4.4. However, it is important to note that the materials used in this study differ from those used in the original verification of the USFD model, which was designed for R8T and UIC60 900A steels. In this work, the mechanical properties were taken from the Manchester Contact Benchmark, which may introduce variations in the estimated wear rates, although this has no effect on the comparison between the two results, which is the purpose of this section.

Figure 22 presents the wear depth values calculated from the results obtained using the FEM and CONTACT for the contact patch of Case 1, right wheel.

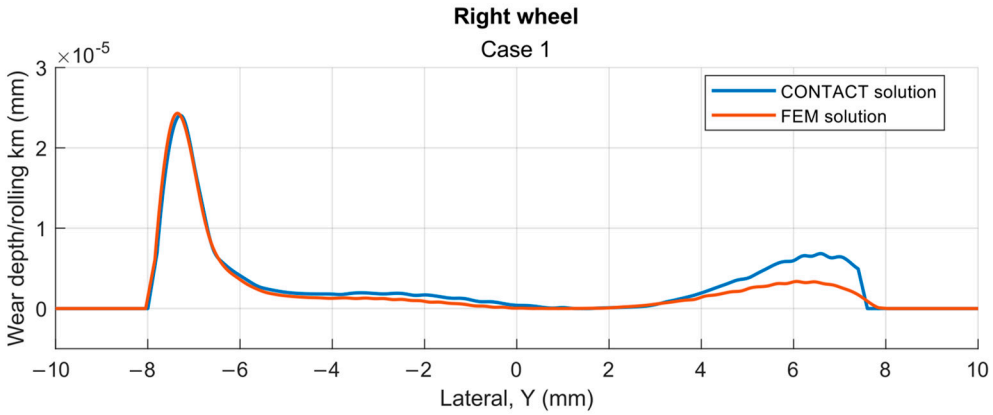


Figure 22. Comparison of CONTACT-FEM wear depth per rolling kilometer. USFD model.

For future studies, the implementation of modified versions of the USFD model tailored to the specific material properties employed in this study is planned, further refining the accuracy of wear estimation.

The quantitative accuracy of wear depth predictions is reported in Supplementary Tables S6 and S7, showing MAE = 4.35 $\times$ 10^{-4} mm/km and RMSE = 6.15 $\times$ 10^{-4} mm/km.

It should be noted that while CONTACT is commonly applied to long-distance extrapolations (up to tens of kilometers), the present FEM simulations are restricted to a few wheel rotations. The validation presented here is therefore local in nature, focusing on contact stresses, slip distributions, and wear increments per rotation rather than long-term profile evolution.

4. Discussion

This study proposes a FEM that proves to be a robust tool for analyzing wheel–rail contact phenomena in detail, capturing effects that are not considered in analytical tools such as CONTACT. The model accurately reproduces contact pressure and contact shear stress, as well as the transition between stick and slip zones under rolling conditions, allowing a detailed analysis of the contact even in the wheel flange. Additionally, wear models can be easily applied from the primary model results, enabling accurate estimates of wheel and rail wear.

The use of a constant wear coefficient K, calibrated for R8T/UIC60 steels, limits the absolute predictive accuracy of wear in this study; however, since both FEM and CONTACT

use the same K, the relative comparison remains valid. Similarly, the strictly elastic material law excludes plasticity and damping effects, which are relevant for long-term wear but outside the scope of the Manchester Benchmark.

The quasi-static implicit formulation employed provides a significant reduction in computational cost compared with transient FEM models, while preserving high accuracy. This makes the framework suitable for large parametric studies requiring multiple simulations. Verification against CONTACT confirms strong agreement: percentage differences in contact pressures, shear stresses, and resultant forces remain within acceptable ranges for nonlinear contact problems. Stick–slip partitions also match closely, with deviations of less than 1.9% in adhesion area across the studied cases.

Observed discrepancies stem from the inherent differences between FEM and CONTACT formulations. FEM explicitly represents the elastic deformation of solids, including three-dimensional and geometric effects such as surface curvature and local stress concentration. CONTACT, based on half-space theory, focuses on local interactions at the interface and does not include global structural deformation, but remains extremely efficient under such assumptions.

The largest deviations occur when the contact patch extends into the wheel flange, where curvature is high and the contact area is small. In such conditions, local stresses are amplified and differences between formulations become more evident. FEM can provide greater accuracy in representing these complex geometries.

During development, mesh refinement and solver strategies were optimized to balance accuracy and efficiency. The final setup achieves an average runtime of ~3 h per case on 20 cores (≈60 core-hours). Although this is more expensive than CONTACT, the combination of refined local meshing and solver parameter tuning reduced runtime by ~40% compared with a uniform fine mesh. This makes computational cost tractable for parametric sweeps and supports the intended application of the model to large design spaces.

The FEM approach becomes particularly advantageous in conditions that challenge half-space formulations, such as flange contact and high yaw angles, where local curvatures are small and stick–slip zones are highly nonlinear. Moreover, FEM naturally incorporates global structural deformation—critical for independently rotating wheelsets or coupled vehicle dynamics—and can be extended to elastoplastic laws and temperature-dependent friction models. These capabilities lie beyond the scope of CONTACT's half-space theory.

As a first application, the model is being used to investigate wheel–rail contact in independently rotating wheelsets, as employed in Talgo trainsets. The framework enables parametric variation in toe and camber angles to evaluate their influence on wear and stability, with the ultimate goal of identifying optimum design values.

It should also be emphasized that the present quasi-static FEM framework is not intended to replace dynamic or thermomechanical FE approaches, which address complementary phenomena such as high-frequency vibrations or temperature-induced degradation. Instead, the proposed methodology is positioned as a computationally efficient tool for large parametric sweeps and IRW-oriented studies, providing accurate elastic contact predictions at a fraction of the cost required by more detailed dynamic or coupled thermo-mechanical analyses.

Future work will extend the methodology towards elastoplastic constitutive laws, calibrated wear coefficients, and profile update strategies, thereby enhancing predictive accuracy for long-term wear while retaining efficiency for large-scale parametric analyses.

5. Conclusions

This work developed and verified a quasi-static FEM framework for wheel–rail contact, systematically benchmarked against the reference software CONTACT. The model accurately

reproduced contact pressures, shear stresses, force components, and stick–slip distributions over the 11 odd-numbered Manchester Benchmark cases (both wheels), with quantified errors (MAE and RMSE) within acceptable limits for nonlinear contact simulations.

The main contributions of this study can be summarized as follows: (i) the development of a quasi-static FEM framework that combines rigid–flexible domain partitioning, a frictionless preconditioning strategy, and automated slip-tolerance tuning, ensuring both accuracy and computational efficiency; (ii) comprehensive verification against CONTACT, including a statistical assessment of errors across normal and tangential variables; and (iii) the establishment of a parametrizable basis for future studies of independently rotating wheels (IRWs), in which geometric variables such as toe and camber angles can be systematically explored, with direct relevance to passive steering concepts in Talgo trainsets.

Limitations include the use of a constant wear coefficient K from literature and a strictly elastic material law, which restricts absolute wear prediction but preserves the validity of relative comparisons. Future work will extend the framework to elastoplastic constitutive laws, calibrated wear coefficients, and profile update strategies, thereby improving predictive accuracy for long-term wear while retaining computational efficiency.

Supplementary Materials: The following supporting information can be downloaded at: https://www.mdpi.com/article/10.3390/vehicles7030104/s1. Supplementary Section S1: Parameters used in the FEM implementation; Supplementary Section S2: Per-case FEM vs. CONTACT relative errors; Supplementary Section S3: Summary statistics; Supplementary Section S4: Wear depth accuracy metrics; Supplementary Section S5: Contact pressure distributions in the contact patch. CONTACT-FEM comparison. Results for Cases 1 to 21; Supplementary Section S6: Longitudinal section view of the contact pressure. CONTACT-FEM comparison. Results for Cases 1 to 21; Supplementary Section S7: Stick/slip zone distributions in the contact patch. CONTACT-FEM comparison. Results for Cases 1 to 21; Supplementary Section S8: Contact shear stress distributions in the contact patch. CONTACT-FEM comparison. Results for Cases 1 to 21; Supplementary Section S9: Longitudinal section view of the contact shear stress. CONTACT-FEM comparison. Results for Cases 1 to 21; Supplementary Section S10: Slip distributions in the contact patch. CONTACT-FEM comparison. Results for Cases 1 to 21; Supplementary Section S11: Longitudinal section view of the slip. CONTACT-FEM comparison. Results for Cases 1 to 21.

Author Contributions: Conceptualization, M.S.-L. and D.A.-L.; methodology, software, validation, formal analysis and investigation, M.G.-T.; resources, M.S.-L. and D.A.-L.; data curation and writing—original draft preparation, M.G.-T.; writing—review and editing, M.S.-L., D.A.-L. and M.G.-T.; visualization, M.G.-T.; supervision and project administration, M.S.-L. and D.A.-L.; funding acquisition, M.S.-L. All authors have read and agreed to the published version of the manuscript.

Funding: This research was funded by Patentes Talgo S.L.U., grant number TALGO1.22I.

Data Availability Statement: The processed numerical results supporting the figures and tables are provided in the Supplementary Materials (Sections S1–S11). The raw finite-element model files (ANSYS Mechanical 24.1), CONTACT 23.2 input decks, and MATLAB R2023a post-processing scripts contain proprietary information and are therefore not publicly available. Subject to a request to the corresponding author and, where necessary, a non-disclosure agreement and permission from the IP owner, access to these raw files can be provided.

Conflicts of Interest: The authors declare no conflicts of interest. The funders had no role in the design of the study; in the collection, analyses, or interpretation of data; in the writing of the manuscript; or in the decision to publish the results. Intellectual-property restrictions concern only the dissemination of raw input files and do not affect the results or conclusions presented in this article.

Abbreviations

The following abbreviations are used in this manuscript:

K_t	Tangential stiffness
F_{K_t}	Tangential stiffness factor
μ	Friction coefficient
p_n	Contact pressure
slto	Elastic slip tolerance
S_{tol}	Dimensionless slip tolerance factor
l_i	Characteristic contact length associated with the size of the finite element
c	Ratio of rolling displacement per time increment (δq) to mesh size (δx)
δq	Ratio of rolling displacement per time increment
δx	Mesh size
δt	Time increment for each integration substep
V	Rolling velocity
F_X, F_Y, F_Z	Forces in the longitudinal, lateral, and normal directions within the contact patch
M_Z	Spin moment within the contact patch
p_I^X, p_I^Y, p_I^Z	Contact shear stresses at node I in the X, Y, and Z components
$\delta_X \cdot \delta_Y$	Element area, the product of its dimensions in the X and Y directions
X_I, Y_I	Distances to the moment application point for node I in the X and Y components
W	Local mass wear rate ($\mu g/m_{rolled}/mm^2$)
K	Empirical wear coefficient specific to the material
T	Local tangential force
γ_x, γ_y	Local slip values in the X and Y directions
A	Local contact area
p_x, p_y	Contact shear stresses in the X and Y directions
i	Position of the element in the strip
j	Longitudinal strip
ρ	Material density
$V\Delta t$	Distance travelled (rolling)
Δx_j	Dimension of the element in the longitudinal and lateral directions
R_j	Rolling radius
D_j	Wear depth in strip j per rolling distance

References

1. Hertz, H. Ueber Die Berührung Fester Elastischer Körper. *J. Reine Angew. Math.* **1882**, *1882*, 156–171. [CrossRef]
2. Hobbs, A.E.W. *A Survey of Creep*; British Railways Research Department, DYNS2: Derby, UK, 1967; pp. 6–9.
3. Nayak, P.R.; Hariharan, S.; Abiock, R.; Marchan, A.P.; Stern, R.; Gupta, P.K. *Friction and Creep in Rolling Contact*; U.S. Department of Transportation, Federal Railroad Administration: Cambridge, MA, USA, 1971; Report No. FRA-RT-71-64.
4. Carter, F.W. On the Action of a Locomotive Driving Wheel. *Proc. R. Soc. Lond. Ser. A Contain. Pap. Math. Phys. Character* **1926**, *112*, 151–157. [CrossRef]
5. Kalker, J.J. *Three-Dimensional Elastic Bodies in Rolling Contact*; Springer: Dordrecht, The Netherlands, 1990.
6. Vollebregt, E.A.H. *User Guide for CONTACT: Rolling and Sliding Contact with Friction*; Version 22.2; Vtech CMCC: Delft, The Netherlands, 2022.
7. Vollebregt, E.A.H. Numerical Modeling of Measured Railway Creep versus Creep-Force Curves with CONTACT. *Wear* **2014**, *314*, 87–95. [CrossRef]
8. Telliskivi, T.; Olofsson, U. Contact Mechanics Analysis of Measured Wheel-Rail Profiles Using the Finite Element Method. *Proc. Inst. Mech. Eng. F J. Rail Rapid Transit* **2001**, *215*, 65–72. [CrossRef]
9. Sladkowski, A.; Sitarz, M. Analysis of Wheel–Rail Interaction Using FE Software. *Wear* **2005**, *258*, 1217–1223. [CrossRef]
10. Iwnicki, S. *Handbook of Railway Vehicle Dynamics*; CRC Press: Boca Raton, FL, USA, 2006. [CrossRef]
11. Vollebregt, E.; Segal, G. Solving Conformal Wheel–Rail Rolling Contact Problems. *Veh. Syst. Dyn.* **2014**, *52* (Suppl. 1), 455–468. [CrossRef]
12. Wei, Z.; Li, Z.; Qian, Z.; Chen, R.; Dollevoet, R. 3D FE Modelling and Validation of Frictional Contact with Partial Slip in Compression–Shift–Rolling Evolution. *Int. J. Rail Transp.* **2016**, *4*, 20–36. [CrossRef]

13. Zhao, X.; Li, Z. A Solution of Transient Rolling Contact with Velocity Dependent Friction by the Explicit Finite Element Method. *Eng. Comput* **2016**, *33*, 1033–1050. [CrossRef]
14. He, C.; Yang, Z.; Zhang, P.; Li, S.; Naeimi, M.; Dollevoet, R.; Li, Z. A Finite Element Thermomechanical Analysis of the Development of Wheel Polygonal Wear. *Tribol. Int.* **2024**, *195*, 109577. [CrossRef]
15. Cho, Y.; Kwak, J. Development of a New Analytical Model for a Railway Vehicle Equipped with Independently Rotating Wheels. *Int. J. Automot. Technol.* **2012**, *13*, 1047–1056. [CrossRef]
16. Dukkipati, R.V.; Swamy, S.N.; Osman, M. Independently rotating wheel systems for railway vehicles—A state of the art review. *Veh. Syst. Dyn.* **1992**, *21*, 297–330. [CrossRef]
17. Bracciali, A. Railway Wheelsets: History, Research and Developments. *Int. J. Railw. Technol.* **2016**, *5*, 23–52. [CrossRef]
18. Megna, G.; Bracciali, A. Gearless Track-Friendly Metro with Guided Independently Rotating Wheels. *Urban Rail Transit* **2021**, *7*, 285–300. [CrossRef]
19. Carballeira, J.; Baeza, L.; Rovira, A.; García, E. Technical characteristics and dynamic modelling of Talgo trains. *Veh. Syst. Dyn.* **2008**, *46* (Suppl. 1), 301–316. [CrossRef]
20. Zulkifli, N.; Azuan, M.A.; Abdul Hamid, N.H.; Kamaruddin, K.A. Three Dimensional Finite Element Analysis on Railway Rail. *IOP Conf. Ser. Mater. Sci. Eng.* **2018**, *429*, 012010. [CrossRef]
21. Zhang, P.; He, C.; Shen, C.; Dollevoet, R.; Li, Z. Comprehensive validation of three-dimensional finite element modelling of wheel–rail high-frequency interaction via the V-Track test rig. *Veh. Syst. Dyn.* **2024**, *62*, 2785–2809. [CrossRef]
22. He, C.; Yang, Z.; Zhang, P.; Dollevoet, R.; Li, Z. Thermomechanical finite element modelling of wheel–rail contact and experimental validation. *Tribol. Int.* **2025**, *209*, 110666. [CrossRef]
23. ANSYS, Inc. *ANSYS Mechanical User's Guide*; Release 2024; ANSYS Inc.: Canonsburg, PA, USA, 2024.
24. Raous, M. *Quasistatic Signorini Problem with Coulomb Friction and Coupling to Adhesion*; Springer: Vienna, Austria, 1999; pp. 101–178. [CrossRef]
25. ANSYS, Inc. *Contact Technology Guide*; Release 12.1; ANSYS Inc.: Canonsburg, PA, USA, 2009.
26. Shackleton, P.; Iwnicki, S.D. *Wheel–Rail Contact Benchmark*; Version 3.0; Rail Technology Unit, Manchester Metropolitan University: Manchester, UK, 2006.
27. Shackleton, P.; Iwnicki, S. Comparison of Wheel–Rail Contact Codes for Railway Vehicle Simulation: An Introduction to the Manchester Contact Benchmark and Initial Results. *Veh. Syst. Dyn.* **2008**, *46*, 129–149. [CrossRef]
28. Le Lez, S.; Arghir, M.; Frene, J. Static and Dynamic Characterization of a Bump-Type Foil Bearing Structure. *J. Tribol.* **2007**, *129*, 75–83. [CrossRef]
29. ANSYS Inc. *ANSYS Theory Reference*; Release 15.0; ANSYS Inc.: Canonsburg, PA, USA, 2013.
30. ANSYS Inc. *ANSYS Mechanical APDL Theory Guide*; Release 15.0; ANSYS Inc.: Canonsburg, PA, USA, 2013.
31. van der Wekken, C.D.; Vollebregt, E.A.H.; Vuik, K. Occurrence and removal of wiggles in transient rolling contact simulation. In Proceedings of the EuroMech Colloquium 578, Lisbon, Portugal, 10–13 April 2017; Ambrósio, J., Schiehlen, W., Pombo, J., Eds.; IDMEC: Lisbon, Portugal, 2017; pp. 1–11.
32. Pombo, J.; Ambrósio, J.; Pereira, M.; Lewis, R.; Dwyer-Joyce, R.; Ariaudo, C.; Kuka, N. Development of a wear prediction tool for steel railway wheels using three alternative wear functions. *Wear* **2011**, *271*, 238–245. [CrossRef]
33. Tassini, N.; Quost, X.; Lewis, R.; Dwyer-Joyce, R.; Ariaudo, C.; Kuka, N. A numerical model of twin disc test arrangement for the evaluation of railway wheel wear prediction methods. *Wear* **2010**, *268*, 660–667. [CrossRef]
34. Braghin, F.; Lewis, R.; Dwyer-Joyce, R.S.; Bruni, S. A mathematical model to predict railway wheel profile evolution due to wear. *Wear* **2006**, *261*, 1253–1264. [CrossRef]
35. Lewis, R.; Kuka, N.; Ariaudo, C.; Dwyer-Joyce, R.; Tassini, N.; Quost, X. Predicting railway wheel wear starting from multi-body analysis: A preliminary study. In Proceedings of the IEEE/ASME/ASCE 2008 Joint Rail Conference, Wilmington, DE, USA, 22–24 April 2008; ASME, pp. 79–87. [CrossRef]
36. Zhang, J.; Sun, S.; Jin, X. Numerical simulation of two-point contact between wheel and rail. *Acta Mech. Solida Sin.* **2009**, *22*, 352–359. [CrossRef]

Disclaimer/Publisher's Note: The statements, opinions and data contained in all publications are solely those of the individual author(s) and contributor(s) and not of MDPI and/or the editor(s). MDPI and/or the editor(s) disclaim responsibility for any injury to people or property resulting from any ideas, methods, instructions or products referred to in the content.